RESEARCH ARTICLE

NANO · MICRO small
www.small-journal.com

Scalable Preparation of High-Quality Microwave-Assisted Reduced Graphene Oxide via Spatial Configuration Engineering

Kaiming Peng, Wenrou Tian, Zhaolong Li, Nannan Ji, Mengwei Li, Wenlong Zhang, Zhenfei Gao, and Jin Zhang**

The non-uniform heating phenomenon in microwave-assisted synthesis of carbon materials has persistently posed a core challenge restricting the realization of industrial-scale applications for microwave technology. Here, an innovative microwave reduction strategy based on spatial configuration engineering is proposed, solving the problem of uneven product quality in the scale-up preparation of microwave-assisted reduced graphene oxide (m-rGO). The corona-discharge-free and fully exposed irradiation areas jointly determine the stability of batch reduction and quality of m-rGO. The quality of the m-rGO is significantly improved by preferential optimization of the process parameters, achieving an I_D/I_G ratio as low as 0.12 and an excellent electrical conductivity of 13486 S m^{-1}, with a yield of ≈70 g per batch. Due to its high conductivity, lightweight, graphene-based materials have emerged as promising candidates in absorption-dominated electromagnetic interference (EMI) shielding fields. A microwave-assisted reduced graphene oxide/polyurethane (m-rGO/PU) film is prepared with a thickness of 90 µm, exhibiting outstanding EMI SE of up to 40 dB in the X-band. This study provides a strategy for mitigating the quality variability associated with microwave heating technology in the scale-up preparation of various advanced carbon materials, facilitating the industrial application of microwave technology.

1. Introduction

Graphene, a 2D material composed of sp^2-hybridized carbon atoms, has garnered significant attention owing to its exceptional physicochemical properties. Benefiting from its outstanding thermal conductivity, graphene serves as an ideal material for thermal management applications.[1,2] The large specific surface area and excellent chemical stability enable its use in energy storage systems.[3] Especially, Graphene's low density, excellent corrosion resistance, and high electrical conductivity make it a highly attractive candidate for next-generation electromagnetic interference (EMI) shielding materials.[4,5] The EMI shielding mechanism involves absorption, reflection, transmission, and multiple reflections. Shielding effectiveness (SE) is dominated by the intrinsic properties of the material.[6] In defense and military applications, particular emphasis is placed on absorption-dominated EMI shielding performance within the 8.2–12.4 GHz frequency range.[7] The fabrication of high-quality graphene is critical for achieving superior EMI SE. In recent years, the preparation of graphene by microwave-assisted methods has attracted widespread interest.[8–12] Compared to traditional thermal and chemical reduction methods,[13–15] microwave-assisted is not only fast and efficient but also environmentally friendly.[16–18] It can convert graphene oxide (GO) into highly ordered and structurally intact m-rGO within 1–2 s

K. Peng, M. Li
Academy for Advanced Interdisciplinary Research
North University of China
Taiyuan 030051, China

K. Peng, W. Tian, Z. Li, N. Ji, W. Zhang, Z. Gao, J. Zhang
Beijing Graphene Institute (BGI)
Beijing 100095, China
E-mail: gaozf-cnc@pku.edu.cn; jinzhang@pku.edu.cn

The ORCID identification number(s) for the author(s) of this article can be found under https://doi.org/10.1002/smll.202505691

DOI: 10.1002/smll.202505691

W. Tian, Z. Li, J. Zhang
School of Materials Science and Engineering
College of Chemistry and Molecular Engineering
Academy for Advanced Interdisciplinary Studies
Beijing Science and Engineering Center for Nanocarbons
Peking University
Beijing 100871, China

Z. Li
State Key Laboratory of High-Efficiency Utilization of Coal and Green Chemical Engineering
College of Chemistry and Chemical Engineering, Ningxia University
Yinchuan 750021, China

W. Zhang
State Key Laboratory of Heavy Oil Processing
China University of Petroleum
Beijing 102249, China

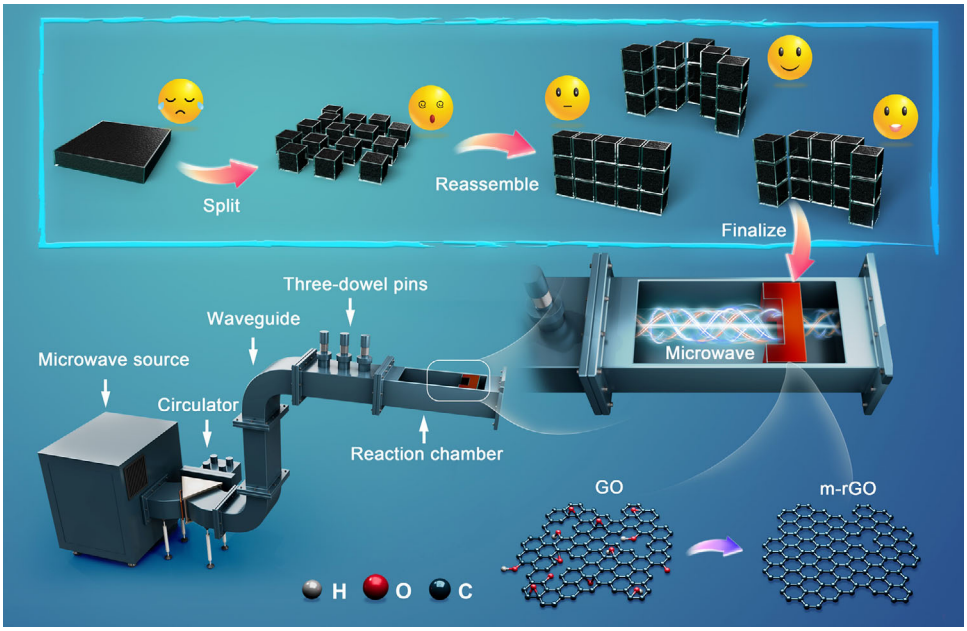

Figure 1. Schematic diagram of the experimental setup, optimized design process, and reduction mechanism for synthesizing reduced graphene oxide via microwave-assisted method.

without the use of any reducing agents,[19] and the electrical conductivity of the resulting m-rGO is significantly enhanced. The reduction mechanism is the rapid temperature increase induced by microwave-material interactions,[20] the high-temperature removal of oxygen-containing functional groups from GO, and the structure defect repaired by free carbon radicals in reaction.[21,22] However, the uneven distribution of the microwave field in the reaction chamber renders the reduction process of GO uncontrollable. This inequality may result in either incomplete reduction of GO or damage to the structural integrity of graphene,[23,24] fundamentally limiting the scale-up production of graphene via microwave-assisted methods.

In order to solve the non-uniform heating phenomenon caused by non-uniform microwave field distribution, researchers have made tremendous efforts. The most straightforward solution is rotating the sample,[25,26] which ensures uniform microwave energy absorption—a method commonly employed in food heating applications. Alternatively, adding multiple microwave sources or utilizing frequency-tunable microwave systems can enhance the uniformity of microwave power within the cavity.[27–29] Additionally, optimizing the structural design of the microwave cavity can further improve the uniformity of electromagnetic fields.[30,31] However, these approaches primarily focus on improving heating uniformity by the microwave field itself and overlook the intrinsic interactions between the material and the microwave energy, which fails to fully address the issue of uneven heating during the process.

Herein, we propose a strategy to improve the quality uniformity of m-rGO by adjusting the spatial distribution of GO in microwave waveguide cavities and designing corresponding irregular-shaped sample containers (**Figure 1**), further improving the quality by systematically optimizing the process parameters in scale-up preparation. Compared with graphene prepared by microwave reduction in other works (Figure S1, Supporting Information), the m-rGO prepared in our work exhibits excellent characteristics, with excellent electrical conductivity (13486 S m^{-1}) and a relatively low Raman D peak intensity (I_D/I_G = 0.12), and the yield can reach ≈70 g per batch. A mechanically flexible microwave-assisted reduced graphene oxide/polyurethane (m-rGO/PU) film with an A4-sized footprint was fabricated via a film applicator, exhibiting a high shielding effectiveness of up to 40 dB in the frequency range of 8.2–12.4 GHz at a thickness of merely 90 µm. This brand-new design concept will provide an innovative and practical method for large-scale industrial production of high-quality m-rGO through microwave radiation technology.

2. Results and Discussion

The scale-up preparation of graphene was performed using a waveguide rectangular 975 (WR975) microwave reaction system (Figure S2, Supporting Information) operating at 915 MHz with an output power of 25 kW (Figure S3, Supporting Information). Before experiments, we first prepared a series of m-rGO with varying degrees of reduction and constructed the relationship between their I_D/I_G and conductivity (Figure S4, Supporting Information). Although Raman spectroscopy is a powerful microscopic analysis technique, its applicability in scale-up preparation experiments is limited. Therefore, there is an urgent need for alternative methods, such as conductivity measurement, to evaluate the reduction quality of powder from a macroscopic perspective. In addition, the electromagnetic field distribution within the waveguide cavity under no-load conditions was numerically simulated. Figure S5 (Supporting Information) illustrates the non-uniform distribution of the electric field within the microwave reactor, where elliptical regions of high electric field intensity and areas of "zero electric field intensity" are observed at specific locations.[32] Given the nonuniform distribution

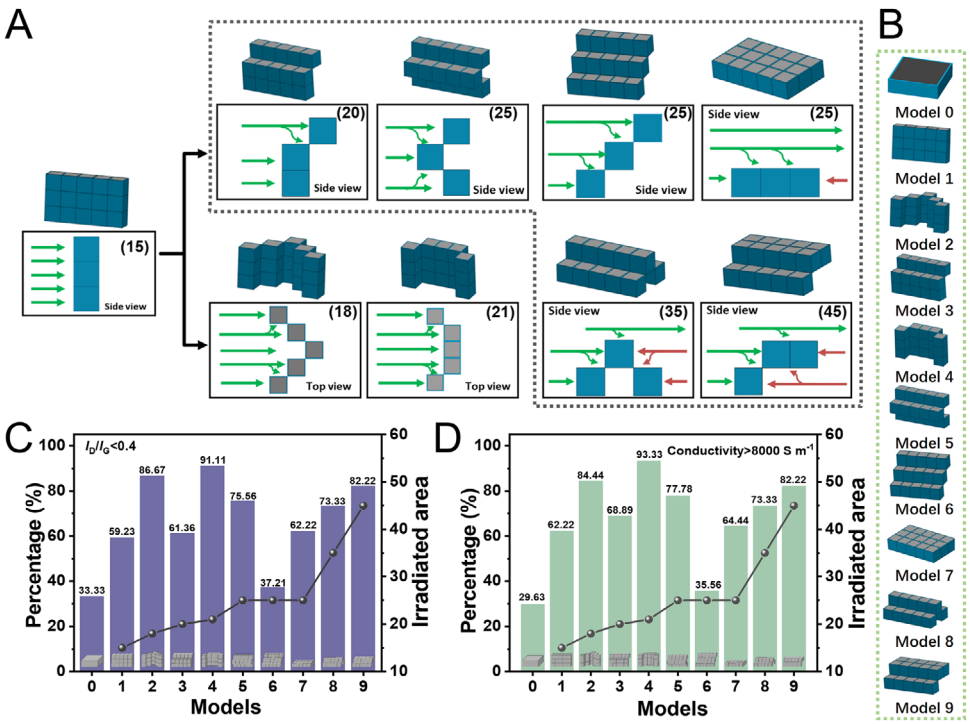

Figure 2. Modeling and experimental results. A) Schematic diagram of model design principles. B) Models legend. C) The percentage of m-rGO with I_D/I_G < 0.4 and (D) conductivity >8000 S m^{-1} in each model.

characteristics of the microwave electric field, we initially investigated the influence of the spatial position of the sample in the microwave field on its reduction efficiency and quality. A quartz transparent container with a size of 160 × 160 × 40 mm was used as the sample container (defined as model 0), which was placed at $\frac{\lambda_g}{4}$ and $\frac{\lambda_g}{2}$ from the terminal metal baffle and processed for 40 s at a microwave power of 25 kW. Here, λ_g denotes the guided wavelength, the calculation method has been mentioned in Figure S5 (Supporting Information).[33] As shown in Figure S6 (Supporting Information), the microwave reduction quality of the GO at $\frac{\lambda_g}{4}$ is significantly better than that at $\frac{\lambda_g}{2}$. The I_D/I_G of the sample obtained at $\frac{\lambda_g}{2}$ are relatively scattered in the range of 0.3–1.0, while those at $\frac{\lambda_g}{4}$ are more concentrated ≈0.4. Therefore, the electric field concentration region located at a distance of $\frac{\lambda_g}{4}$ from the tail, baffle is considered as the optimal location for microwave-assisted reduction of GO. However, the quality of m-rGO still exhibits significant non-uniformity, mainly reflected in spatial distribution. The presence of the terminal metal baffle induces multiple microwave reflections between the baffle and samples, resulting in enhanced microwave energy absorption by samples proximal to the baffle. This consequently leads to a lower I_D/I_G ratio in these samples compared to those positioned distally from the baffle.

In microwave heating systems, for thin samples where $N_w \leq 0.1$ (N_w represents the relative size of the sample compared to the microwave wavelength), heating is uniform across the sample and the influence of shape on microwave heating can be neglected. However, for samples where $N_w > 0.1$, the interaction between the microwaves and the sample is significantly affected by the thickness and shape of the sample. In this study, the $N_w > 4$, so geometric effects need to be explicitly considered in microwave treatment optimization.

The formula for calculating N_w:[34]

$$N_w = \frac{a}{\lambda_m} \tag{1}$$

$$\lambda_m = \frac{c\sqrt{2}}{f\left[\sqrt{\left(\varepsilon_r'\right)^2 + \left(\varepsilon_r''\right)^2} + \varepsilon_r'\right]^{1/2}} \tag{2}$$

where λ_m is the wavelength of the microwave within the material, ε_r' represents the material's ability to store electric field energy, ε_r'' represents the material's ability to dissipate electric field energy, a is the side of the rectangular container, c is the speed of light, and f is the microwave frequency.

To improve the uniformity of sample heating, we enhanced the microwave–sample interaction through an innovative geometric design of the sample container, aiming to achieve a structural configuration with improved microwave absorption efficiency—defined as the ratio of the difference between the emitted and reflected microwave power to the emitted power. Unlike the traditional cuboid or cylindrical ones, we propose a modular design approach, which enables flexible configuration and adaptive modification of the model architecture. We subdivided model 0 into 15 equally sized (40 × 40 × 40 mm) small square containers (defined as model 1, **Figure** 2A,B). The main principle in designing their arrangement and combination is to maximize the

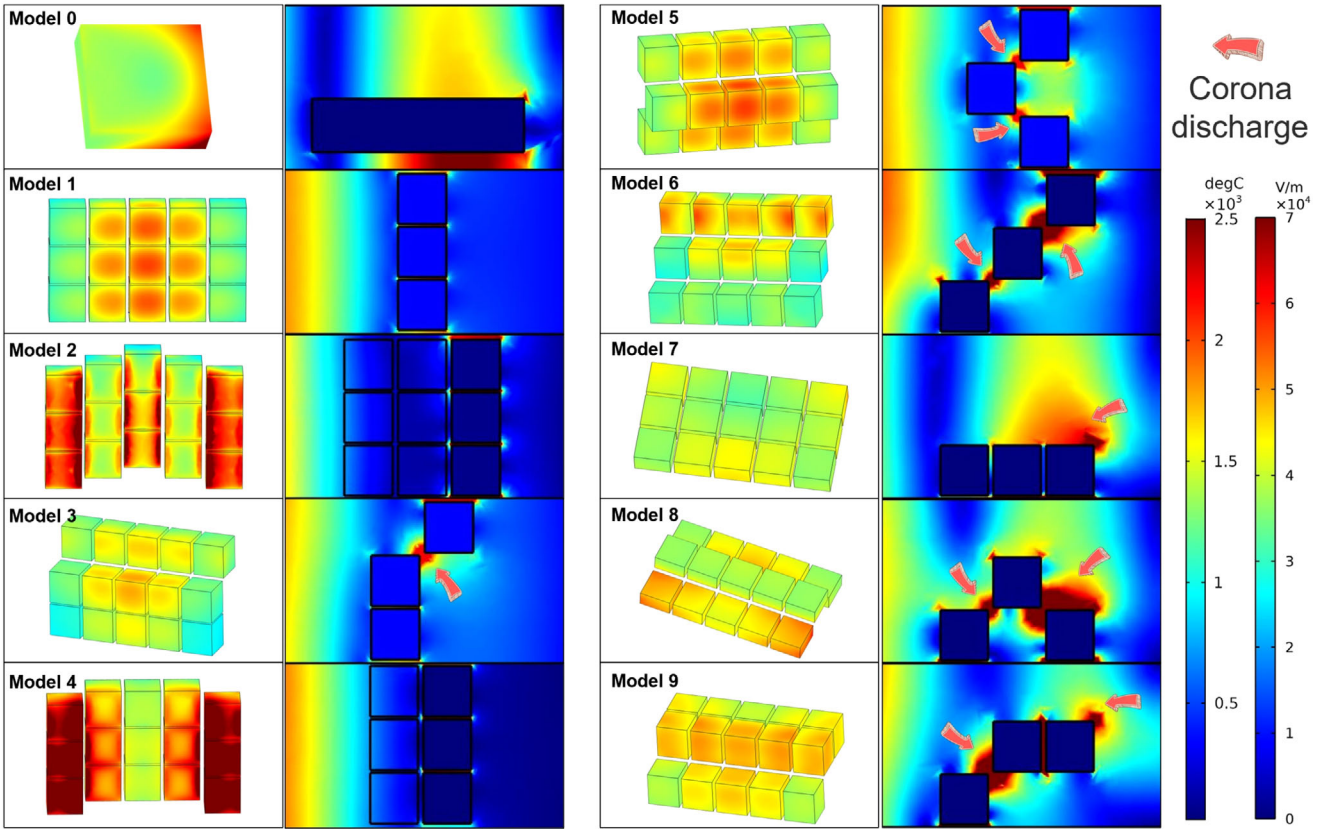

Figure 3. Numerical simulation of electromagnetic-thermal coupling field results for models 0–9 (15 kW, 40 s).

effective interaction areas between the sample and the microwave electromagnetic field, thereby achieving excellent heating uniformity. Additionally, to mitigate the influence of accidental results of individual modules throughout the experimental procedure, a centrally symmetrical layout was adopted to enhance mutual validation between modules within the model.

As shown in Figure 2A, structured adaptations were carried out on the row and column directions relative to the microwave propagation vector based on model 1, ultimately generating nine distinct geometric configurations. The number in parentheses represents the area of the model that can receive microwave radiation and defines the model names in Figure 2B. The green arrows indicate the microwaves irradiating the sample directly, while the orange arrows represent the microwaves irradiating the sample after reflection from the end baffle. The microwave reduction experiments of the designed models were performed under the conditions of microwave power of 15 kW for 40 s with the nitrogen flow rate of 5 L min^{-1}. The quality of the m-rGO was characterized using Raman spectroscopy and a four-point probe powder resistivity meter (Figure 2C,D). Compared with model 0, the uniformity of reduction quality was improved to varying degrees in all models, and model 4 exhibited the best reduction quality. The proportion of samples with conductivity above 8000 S m^{-1} reached 93.33% and I_D/I_G below 0.4 for 91.11% of the samples (Table S1, Supporting Information).

It was observed that increasing the area of the sample exposed to microwave radiation improves the uniformity of the reduction quality. However, this relationship was not strictly linear. Further analysis reveals that the microwave irradiation areas consist of perpendicular surfaces (aligned with the microwave electric field vector) and parallel surfaces (orthogonal to the propagation direction), with the former having a significantly greater effect on heating uniformity. This can be attributed to the fact that the surfaces perpendicular to the microwave direction possess a higher microwave absorption capacity.[34] As shown in Table S2 (Supporting Information), although model 5 and model 7 have the same total microwave irradiation areas, model 5 exhibits superior reduction uniformity due to its larger perpendicular areas. However, this discovery cannot fully explain certain phenomena. The parallel and vertical irradiation areas of model 8 are larger than those of model 4, but its reduction quality is inferior, indicating the existence of other crucial influencing factors. The poor quality of its reduction indicates that there are other crucial factors that need to be considered.

In order to reveal potential influences, electromagnetic-thermal coupling simulations were conducted by COMSOL for each model (**Figure 3**). By analyzing the electric field distribution of different models, it was found that corona discharge is another crucial influencing factor. The ions and electrons generated by the corona discharge migrate within the electric field and form a layer of charge. This layer partially shields the external electric field, resulting in a decrease in the local electric field intensity and a change in the overall electric field distribution.[35] Therefore, corona discharge will have a negative impact on the

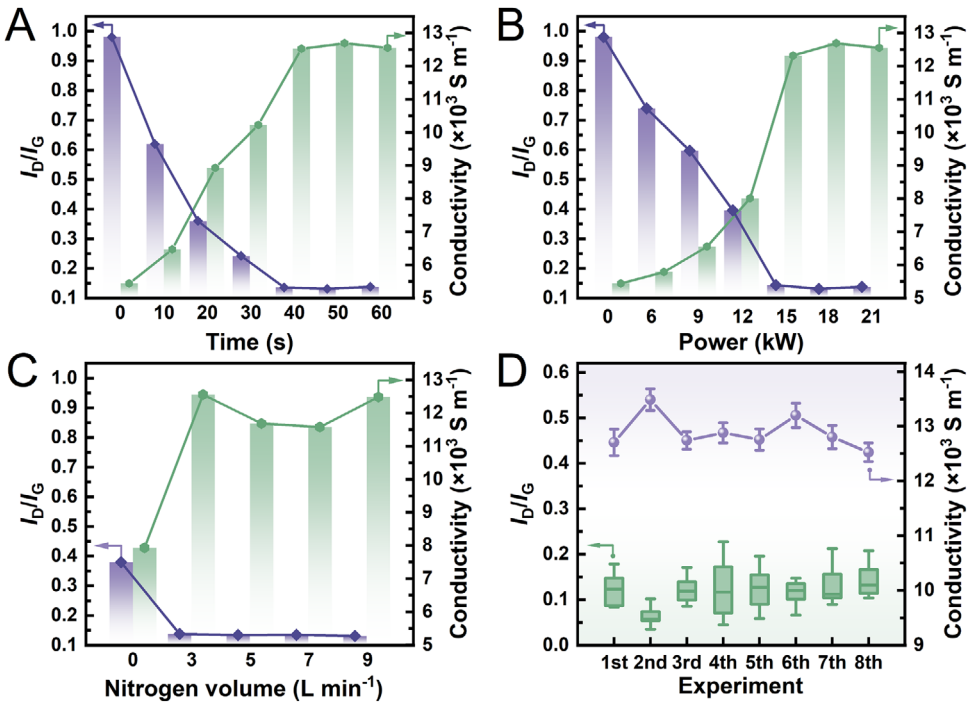

Figure 4. Process control and batch stability under optimal modeling conditions. A) The reduction quality of m-rGO at different adjustment times. The influence of (B) power and (C) nitrogen flow on the reduction quality. D) Batch stability of the reduction quality.

uniformity of microwave reduction. For example, although the total microwave irradiation areas of model 3 and model 4 are similar, the reduction uniformity of model 3 is significantly lower due to the presence of corona discharge effects within the model. In addition, the higher the electric field intensity in the corona discharge region, the greater the adverse effect on reduction quality. Model 5 and Model 6 have identical perpendicular and parallel microwave irradiation areas and the same number of corona discharge regions; however, the microwave reduction quality of Model 5 is better than Model 6. Similarly, model 5 exhibits comparable electric field intensities in the corona discharge regions and an identical number of microwave irradiation areas as model 7, but demonstrates a superior reduction quality. By comparing their compositions of microwave irradiation areas and corona discharge regions, it can be concluded that under these conditions, the effect of perpendicular exposed surfaces on uniformity of microwave heating surpasses that of corona discharge. However, since the effect of corona discharge on heating uniformity depends on both the intensity and number, it is difficult to directly quantify the relative contributions of corona discharge as well as parallel or vertical exposed surfaces to sample heating uniformity (More detailed information supplied in Table S2, Supporting Information).

By comparing the absorption efficiency, average temperature and I_D/I_G of each model in Table S3 (Supporting Information), the level of interaction between each model and the microwave field within the waveguide can be more directly assessed. Table S3 indicates that the higher microwave absorption efficiency of the model corresponds to a higher average temperature, leading to improved quality of the m-rGO. This relationship is more intuitively illustrated in Figure S7 (Supporting Information). Furthermore, a comparative analysis of the thermal field simulation results across different models enables a clearer evaluation of the microwave reduction effect of each model. The simulation results exhibited strong consistency with the experimental observations. Notably, model 4 demonstrated the most extensive temperature distribution above 1500 °C and achieved a higher average temperature within this range. Furthermore, as presented in Table S1, the thermal field distribution trends within model 4 exhibited a positive correlation with the quality of m-rGO, indicating that higher temperatures reached within a shorter heating duration could significantly enhance the reduction degree of GO. Based on the combined findings from simulations and experiments, model 4 was ultimately chosen as the optimal model for subsequent microwave process adjustments.

Based on the structural framework of model 4, a special container was designed and developed in this study (Figure S8, Supporting Information). Compared to model 4, this container incorporates three small cubic compartments on each side, effectively increasing the total volume while maintaining the microwave irradiation area unchanged. This optimization enables the maximum loading capacity of the container to reach 70 g while simplifying the structural design of the formed container and minimizing manufacturing costs.

In order to further improve the reduction quality and uniformity of GO, a systematic control was carried out to optimize the reduction process parameters. First, time-gradient experiments were conducted under constant microwave power (15 kW) and nitrogen flow rate (5 L min^{-1}). As shown in **Figure** 4A, a positive correlation between the reduction quality and microwave exposure time in the range of 0–40 s, with the optimal value being reached at 40 s. However, when the time exceeds 40 s, there

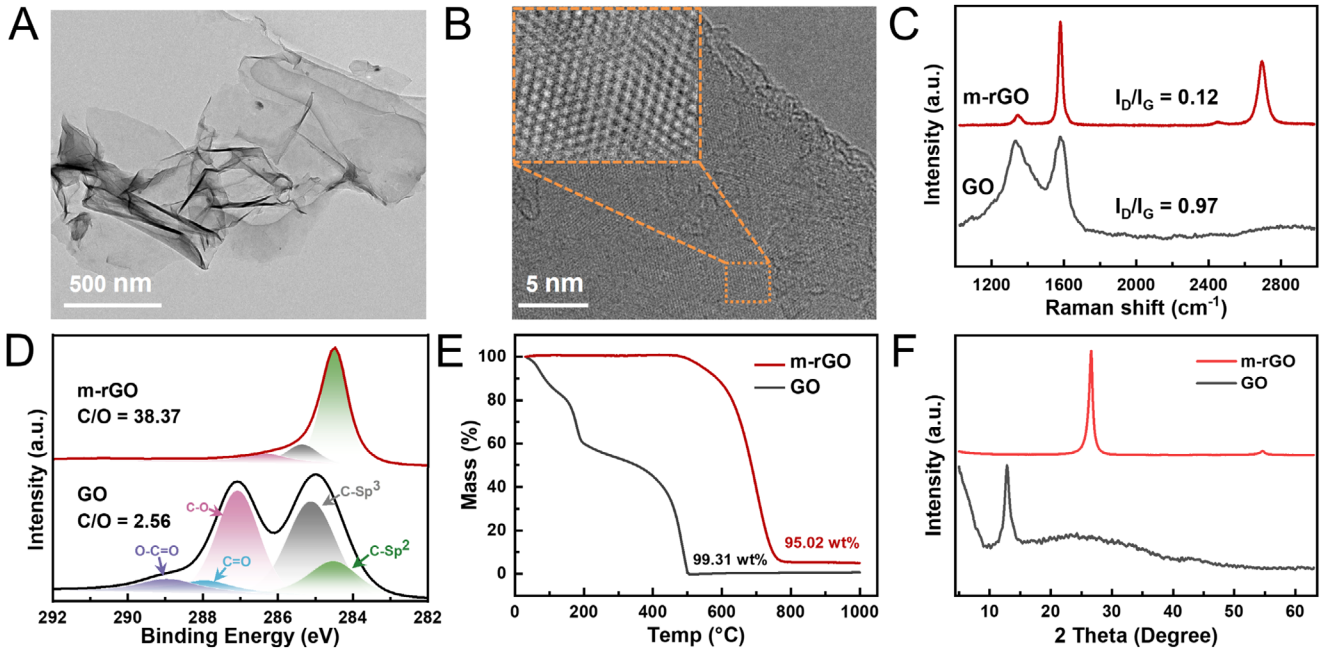

Figure 5. The characterization of prepared m-rGO. A) TEM image of m-rGO. B) High magnification TEM image of m-rGO with a locally magnified region shown in the inset, and the inset has been processed using Fourier transform (FT) and inverse Fourier transform (IFT). C) Raman, D) XPS, E) thermogravimetric analysis (TGA), F) and XRD spectra of GO and m-rGO.

was no significant improvement in the reduction quality. Subsequently, the influence of microwave power on the reduction quality of GO was investigated at fixed irradiation times and atmospheric conditions. Figure 4B indicated that the reduction quality of GO was significantly enhanced with the increase in microwave power. Moreover, the optimum average conductivity of the sample reached at 15 kW, corresponding to an I_D/I_G as low as 0.14. As the microwave power continued to increase further, the reduction quality failed to improve anymore. This might be ascribed to the simultaneous occurrence of the defect repair and carbon skeleton fracture processes in GO at high power levels, with their respective rates reaching an equilibrium state. The results showed that the reduction quality increased significantly with increasing microwave power, with the optimum average conductivity and defect density of the sample being reached at 15 kW. In the absence of inert gas (nitrogen) protection, the electrical conductivity of m-rGO was only 7936 S m^{-1} (Figure 4C). When the nitrogen flow rate was increased to 3 L min^{-1}, a significant improvement in m-rGO quality was observed (conductivity >11500 S m^{-1}). However, further increases beyond this flow rate demonstrated no substantial improvement in quality. It indicates that an inert atmosphere plays a crucial role in effectively suppressing the oxidation or etching of m-rGO and the impact of gas flow rate on reduction quality is relatively minor, low flow conditions are adequate for achieving high-quality reduction. Based on the systematic analysis of the experimental results, combined with economic considerations, the optimal process parameters were determined as microwave power of 15 kW, an irradiation time of 40 s, and an inert gas flow rate of 3 L min^{-1}. The reduction quality of m-rGO prepared using the optimal process parameters was evaluated through multiple experiments to verify its stability (Figure S9, Supporting Information). As shown in Figure 4D, the reduction quality of m-rGO remained stable, the I_D/I_G stayed below 0.14, and the powder conductivity remained higher than 12 500 S m^{-1}. Additionally, to assess the universality of the proposed synthesis approach, GO obtained from various suppliers was treated using the same microwave reduction process. Raman spectroscopy revealed that GO from all sources was successfully reduced to m-rGO (Figure S10, Supporting Information).

To further evaluate the quality of the prepared m-rGO, various physicochemical properties were characterized. **Figure** 5A shows the transmission electron microscopy (TEM) image of m-rGO. Compared to the GO (Figure S11, Supporting Information), the m-rGO shows a clear lattice structure and thickness of ≈5 layers (Figure 5B). The inset also shows a well-ordered graphene structure with an intact lattice arrangement. Figure S12 (Supporting Information) shows the scanning electron microscope (SEM) image of m-rGO. In addition, Raman spectroscopy analysis indicates a significant improvement in structural integrity.[36] The intensity of the D band significantly decreased, and the I_D/I_G decreased from 0.97 to 0.12 (Figure 5C). It suggests that the sp^3 defects within m-rGO are mostly transformed into sp^2 atomic domains upon microwave irradiation.[37]

The X -ray photoelectron spectroscopy (XPS) survey spectra of the sample show that it mainly consists of C1s and O1s peaks located at 284.5 and 532 eV, respectively (Figure S13, Supporting Information). The spectrum of GO exhibits a distinct oxygen peak, while it almost disappears in the m-rGO and its spectral features are similar to those of graphene synthesized by chemical vapor deposition (CVD). To further investigate the distribution of functional groups in GO, m-rGO and graphene, the C1s peak was subjected to deconvolution, which can be deconvoluted into five peaks at 284.8, 285.5, 286.6, 287.5, and 288.7 eV, corresponding to C=C, C—C, C—O, C=O and O—C=O,

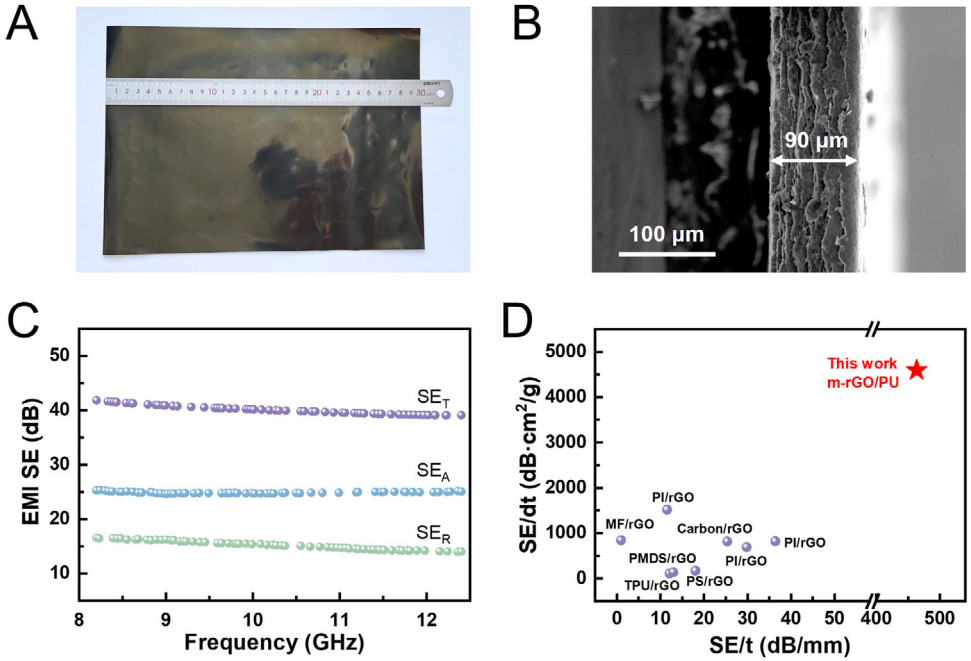

Figure 6. A) Photograph of the m-rGO/PU film. B) SEM image and (C) EMI SE of m-rGO/PU film. D) Comparison of the EMI SE of the m-rGO/PU films with that reported in other literature.

respectively (Figure 5D). GO mainly contains a large number of epoxy and hydroxyl groups, along with a small amount of carbonyl and carboxyl groups, with a carbon/oxygen ratio of 2.56. In contrast, m-rGO contains only C═C, C—C, and C—O, and the peaks of C #x0003D; O and O—C═O disappear, indicating that most of the oxygen-containing groups have been removed with a C/O ratio of 38.37.

The mass loss characteristics of GO were divided into three main stages according to the temperature changes (Figure 5E). The first stage corresponds to the removal of free water (<100 °C), the second stage is associated with the decomposition of oxygen-containing functional groups (100–360 °C) and the third stage pertains to the sp^2 decomposition of sp^2 carbon (360–1000 °C). The derivative thermogravimetric analysis curve reveals that the mass of m-rGO remains relatively stable within the temperature range of 30–500 °C (Figure S14, Supporting Information). This phenomenon indicates that most of the oxygen-containing functional groups in GO have been removed after microwave treatment. Furthermore, the disappearance of the 2θ diffraction peak ≈12.3° in the X-ray diffraction (XRD) spectrum of m-rGO further confirms this conclusion (Figure 5F).

Based on the high electrical conductivity of m-rGO, we blended the prepared m-rGO with PU solution to fabricate high-quality m-rGO/PU EMI films, as shown in **Figure** 6A. The resulting film has an A4-sized area and an average thickness of 90 μm. The cross-sectional SEM image shows a densely packed multilayered structure of the m-rGO/PU film (Figure 6B). This structure enables multiple internal reflections and absorptions of incident electromagnetic waves, significantly enhancing the film's EMI SE. With a conductivity of 422 S m^{-1}, the film exhibits absorption-dominated EMI shielding behavior across the X-band frequency range, as shown in Figure 6C. Despite its thinness (90 μm), the composite achieves a total EMI SE of 40 dB, corresponding to 99.99% attenuation of electromagnetic waves, demonstrating its significant potential for commercial applications. Moreover, the specific shielding effectiveness divided by sample thickness (SE/t) and divided by sample density and thickness (SE/dt) of m-rGO/PU film reached 463.4 dB mm^{-1} and 4593.4 dB cm^2 g^{-1}, respectively, which is higher than that of other rGO-based polyurethane composites recently reported (Figure 6D).[38–45] It suggests that m-rGO/PU can be applied as EMI shielding ink to coat electronic devices.

3. Conclusion

To address the issue of product quality consistency and stability in the large-scale preparation of graphene through microwave-assisted methods, we adopt a modular research approach and optimize the spatial configuration of GO to maximize the utilization of microwave energy. Based on the preferred spatial layout structure, we designed and customized the corresponding irregular-shaped sample container. Subsequently, we further adjusted the microwave process parameters and carried out repeated experiments, successfully achieving stable scale-up preparation of high-quality m-rGO powder with a yield of 70 g per batch. The average I_D/I_G of the prepared sample decreased to 0.12, and the conductivity reached 13486 S m^{-1}. Based on its high conductivity and low density, we applied it to electromagnetic shielding to evaluate its electromagnetic shielding effectiveness. The m-rGO/PU film prepared in this work shows excellent conductivity of 422 S m^{-1}, and X-band EMI SE of 40 dB at a thickness of 90 μm. This study provides a practical strategy for the uniform synthesis of high-quality nanomaterials via microwave methods; it also carries

important significance implications for advancing the application of graphene materials in EMI.

4. Experimental Section

Materials: The sample 1 (GO) used in this work was purchased from Baotailong Co., Ltd., sample 2 (GO-Z) was purchased from Zhongke Yueda (Shanghai) Materials Technology Co., Ltd. and sample 3 (GO-A) was obtained from Angxing Advanced Carbon Materials Co., Ltd. The raw GO was pretreated at 300 °C for 30 min to improve its electrical conductivity and microwave absorption performance. The pretreated sample 1 (GO) was characterized, consisting of ≈5–8 layers (Figures S11 and S15, Supporting Information), with a conductivity of 5500 S m^{-1}, relative permittivity (ϵ) of 14.3, lateral size of 8–10 µm (Figure S12, Supporting Information), and $I_D/I_G \approx 1$ (Figure 5C). The polyurethane (PU) polymer-water emulsion (PU-2590, 45% solid content) was obtained from Dongguan Xinmiao New Materials Co., Ltd. Polyvinylpyrrolidone (PVP) was from Beijing Innochem Technology Co., Ltd (average Mw 40000, K30).

Preparation of m-rGO/PU Film: A total of 30 g of m-rGO, 3 g of PVP, 250 g of deionized water, and 283 g of stainless-steel balls were mixed and subjected to ball milling for 12 h. Subsequently, 156 g of PU was added to the mixture, followed by an additional 30 min of ball milling to obtain the m-rGO slurry. m-rGO slurry was uniformly coated onto a substrate using a film applicator and allowed to dry naturally at room temperature for 36 h. The final films obtained were denoted as m-rGO/PU.

Characterization: SEM was employed to characterize the dimensional features of m-rGO. TEM (Tecnai G2 F30) was employed to characterize the microstructure of GO and m-rGO, respectively. The surface chemical composition was analyzed using XPS (Thermo Scientific K-Alpha), with the binding energies in the high-resolution spectra calibrated by setting the C1s peak to 284.5 eV. XRD (D8 ADVANCE) was used to determine the physical phase and crystal structure of the samples. Raman spectroscopy (LabRAM HR Evolution) was utilized to evaluate the structural integrity of GO and m-rGO (Laser wavelength: 532 nm, power: 50%, integration time: 10 s, accumulation: 2.), and the final result for each sample is the average of three test results. TGA (STA 449 F5) and derivative thermogravimetric were conducted to assess the thermal weight loss characteristics and determine the content of individual components by measuring the mass change of the samples with respect to temperature or time.

Conductivity Testing: The resistivity (ρ) of the samples was measured using a four-point probe resistivity measurement system for powders (ST2722-SD). The four-point probe method is based on Ohm's law and utilizes four probes, where the current is introduced through the outer probes and voltage is sensed by the inner probes, effectively eliminating the influence of contact resistance. ST2722-SD is capable of automatically correcting the thickness factor during the powder compaction process, thereby ensuring accurate resistivity calculations. The electrical conductivity (σ) was calculated as the reciprocal of the resistivity, i.e., $\sigma = 1/\rho$. Before each test, all m-rGO powder was thoroughly mixed, and three positions were randomly selected for sample collection, each weighing 20 mg. After the sample was transferred to the mold, set the pressure to 3 MPa and record the resistivity value after the resistivity measurement in stabilized conditions. Ultimately, the average value of the three measurements was displayed as the final result.

Microwave Reduction Experiment: The WR975 system was used for the scale-up preparation of m-rGO (Figure S2, Supporting Information). The operating frequency of the device is 915 MHz, the power range is 5–25 kW (Figure S3, Supporting Information), the quartz container are used as reaction vessels, and the nitrogen gas is used as the inert atmosphere. Before starting the microwave, the quartz containers were purged with nitrogen at a flow rate of 10 L min^{-1} for 3 min. During microwave irradiation, the flow rate decreases to 3 L min^{-1}. After irradiation, nitrogen purge was continued at a rate of 3 L min^{-1} for 3 min to promote cooling and collect samples for subsequent characterization.

COMSOL Simulation Method: The electromagnetic-thermal coupling simulations were performed using the microwave heating module in COMSOL Multiphysics. To simplify the computation and enhance efficiency, the following assumptions were made:

Sample Properties: Assuming the GO powder was a solid material with isotropic and homogeneous properties.

Dielectric Parameters and Electrical Conductivity: The dielectric constant and electrical conductivity were assumed to remain constant. The microwave reaction process is often characterized by ultra-short duration and high temperature, posing significant challenges to existing measurement techniques for capturing real-time changes in dielectric constant and conductivity. Consequently, this study does not explore theoretical aspects but focuses on analyzing the temperature gradient trend within the model.

Heat Transfer Mechanism: Heat transfer was assumed to occur only via conduction within the sample and radiation from the sample surface to the surrounding air, while convective heat transfer was neglected. This simplification is justified by the short experimental duration, the low carrier gas flow rate, and the significantly lower thermal conductivity of the carrier gas compared to GO powder, rendering the convective heat transfer effect negligible.

The numerical simulations in this paper utilize an electromagnetic-thermal linear model, and the key parameters involved are as follows:

Relative permittivity (ϵ): 14.3
Relative permeability (μ): 1.05
Electrical conductivity (σ): 5500 S m^{-1}
Thermal conductivity (K): 10 W m^{-1} K^{-1}
Heat capacity at constant pressure (Cp): 670 J kg^{-1} K^{-1}
Density (ρ): 5.6 kg m^{-3}

Measurements and Theoretical Calculations of EMI Shielding: The relative permittivity of GO and the scattering parameters (S_{11}, S_{12}, S_{22}, and S_{21}) of m-rGO were measured using a vector network analyzer (PNA-N5244A).

The EMI SE Typically Consists of Three Components: Absorption (SE_A), reflection (SE_R), and multiple internal reflections or scattering (SE_{RM}). When SE_T>10 dB, the SE_M can be neglected. The total EMI SE (SE_T) can be expressed as:

$$SE_T = SE_A + SE_R + SE_{MR} \quad (3)$$

The transmittance (T), reflectance (R), A (absorbance), SE_A, SE_R, and SE_{RM} of samples were calculated by Equations (4)–(9):[46]

$$T = |S_{21}|^2 = |S_{21}|^2 \quad (4)$$

$$R = |S_{11}|^2 = |S_{22}|^2 \quad (5)$$

$$A = 1 - R - T \quad (6)$$

$$SE_T = -10 \log T \quad (7)$$

$$SE_R = -10 \log (1 - R) \quad (8)$$

$$SE_A = 10 \log \left(\frac{1 - R}{T} \right) \quad (9)$$

Supporting Information

Supporting Information is available from the Wiley Online Library or from the author.

Acknowledgements

This work was financially supported by the Ministry of Science and Technology of China (2022YFA1203302, 2022YFA1203304 and 2018YFA0703502), the National Natural Science Foundation of China (Grant Nos.

T2188101, 52021006), the Strategic Priority Research Program of CAS (XDB36030100), the Beijing Nova Program (20240484491), the Beijing National Laboratory for Molecular Sciences (BNLMS-CXTD-202001) and the Shenzhen Science and Technology Innovation Commission (KQTD20221101115627004).

Conflict of Interest

The authors declare no conflict of interest.

Author Contributions

K.P., W.T., and Z.L. contributed equally to this work. The project was conceived and supervised by J.Z. and Z.G., K.P. prepared m-RGO and conducted the initial draft preparation with assistance from W.T. in data collection and organization. Numerical simulations were performed under the guidance of M.L., Z.L., and N.J. contributed to the characterization tests and jointly established the experimental platform with K.P., W.Z. led the experiments for the application part. All authors have critically reviewed the manuscript and approved the final version.

Data Availability Statement

The data that support the findings of this study are available from the corresponding author upon reasonable request.

Keywords

electromagnetic interference shielding, microwave heating, numerical simulation, reduced graphene oxide, scale-up preparation

Received: May 11, 2025
Revised: June 18, 2025
Published online: July 11, 2025

[1] J. X. Wang, Y. Mao, N. Miljkovic, *Adv. Sci.* **2024**, *11*, 2402190.
[2] J. Hu, Y. Hu, J. Yang, Y. Ye, R. Shen, *Chem. Eng. J.* **2023**, *476*, 146670.
[3] R. Fang, K. Chen, L. Yin, Z. Sun, F. Li, H. M. Cheng, *Adv. Mater.* **2019**, *31*, 1800863.
[4] J. Zhang, T. Xu, L. Ding, J. Ji, J. Geng, H. T. Ngo, K. Zhou, X. Chen, F. Geng, *eScience* **2025**, https://doi.org/10.1016/j.esci.2025.100407.
[5] B. Hu, H. Guo, J. Li, T. Li, M. Cao, W. Qi, Z. Wu, Y. Li, B. Li, *Composites, Part B* **2023**, *266*, 110998.
[6] C. Wen, K. Lan, M. Ding, S. Bai, J. Jing, D. Xu, *Colloids Surf., A* **2025**, *711*, 136403.
[7] Z. Ma, R. Jiang, J. Jing, S. Kang, L. Ma, K. Zhang, J. Li, Y. Zhang, J. Qin, S. Yun, *Nano-Micro Lett.* **2024**, *16*, 223.
[8] O. Park, N. H. Kim, J. H. Lee, *Carbon* **2022**, *187*, 330.
[9] R. Kumar, E. T. da Silva, R. K. Singh, R. Savu, A. V. Alaferdov, L. C. Fonseca, L. C. Carossi, A. Singh, S. Khandka, K. K. Kar, *J. Colloid Interf. Sci.* **2018**, *515*, 160.
[10] J. Shen, T. Li, Y. Long, M. Shi, N. Li, M. Ye, *Carbon* **2012**, *50*, 2134.
[11] J. Li, Z. Yang, H. Qiu, Y. Dai, Q. Zheng, G. Zheng, J. Yang, *J. Mater. Chem. A* **2013**, *1*, 11451.
[12] S. Yetiman, H. Peçenek, F. K. Dokan, M. S. Onses, E. Yılmaz, E. Sahmetlioglu, *J. Energy Storage* **2022**, *49*, 104103.
[13] D. R. Dreyer, S. Park, C. W. Bielawski, R. S. Ruoff, *Chem. Soc. Rev.* **2010**, *39*, 228.
[14] T. Soltani, B. Lee, *J. Colloid Interf. Sci.* **2017**, *486*, 337.
[15] J. Guo, B. Mao, J. Li, X. Wang, X. Yang, *Carbon* **2021**, *171*, 963.
[16] S. Park, R. S. Ruoff, *Nat. Nanotechnol.* **2009**, *4*, 217.
[17] C. H. A. Wong, O. Jankovský, Z. Sofer, M. Pumera, *Carbon* **2014**, *77*, 508.
[18] J. Guan, S. Zhou, J. Zhou, F. Wu, X. Shi, J. Xu, L. Shao, Z. Luo, Z. Sun, *ACS Appl. Mater. Interfaces* **2024**, *16*, 20559.
[19] D. Voiry, J. Yang, J. Kupferberg, R. Fullon, C. Lee, H. Y. Jeong, H. S. Shin, M. Chhowalla, *Science* **2016**, *353*, 1413.
[20] R. R. Mishra, A. K. Sharma, *Composites, Part A* **2016**, *81*, 78.
[21] M. Guo, H. Yuan, K. Ni, C. Ye, F. Pan, J. Xiong, Y. Zhu, *Adv. Sci.* **2025**, *12*, 2410088.
[22] S. Pei, H. Cheng, *Carbon* **2012**, *50*, 3210.
[23] Z. Li, Y. Yao, Z. Lin, K. Moon, W. Lin, C. Wong, *J. Mater. Chem.* **2010**, *20*, 4781.
[24] E. F. Rahayu, B. Bunnari, A. Hardyansyah, *Molekul* **2020**, *15*, 56.
[25] H. Zhu, J. He, T. Hong, Q. Yang, Y. Wu, Y. Yang, K. Huang, *Appl. Therm. Eng.* **2018**, *141*, 648.
[26] J. He, Y. Yang, H. Zhu, K. Li, W. Yao, K. Huang, *Appl. Therm. Eng.* **2020**, *178*, 115594.
[27] J. Zhou, Y. Li, N. Li, S. Liu, L. Cheng, S. Sui, J. Gao, *Composites, Part A* **2018**, *107*, 10.
[28] C. Wang, Z. Peng, F. Yang, H. Zhu, L. Yan, C. Stud, *Therm. Eng.* **2024**, *61*, 104919.
[29] R. Yang, J. Chen, *Food Res. Int.* **2024**, *175*, 113781.
[30] H. Zhao, H. Li, X. Li, X. Gao, *Appl. Therm. Eng.* **2021**, *197*, 117346.
[31] F. Huang, T. Wang, S. Wu, T. Li, *Chem. Eng. J.* **2024**, *500*, 156950.
[32] L. Ren, K. Zhang, F. Wang, Y. Zhang, F. Yang, F. Cheng, *Chem. Eng. J.* **2023**, *470*, 143975.
[33] D. M. Pozar, in *Microwave Engineering*, John Wiley & Sons, Nashville, TN **2012**, p. 3.
[34] M. Bhattacharya, T. Basak, *Innovative Food Sci. Emerg. Technol.* **2017**, *39*, 247.
[35] M. Becerra, V. Cooray, S. Soula, S. Chauzy, *J. Geophys. Res.: Atmos.* **2007**, *112*, D12205.
[36] J. Li, J. Liu, N. Li, W. Zeng, M. Chen, Y. Xu, *Carbon* **2025**, *235*, 120081.
[37] Z. Xiong, P. Yu, Q. Liang, D. Li, *Sci. China Mater.* **2023**, *66*, 4733.
[38] P. R. Agrawal, R. Kumar, S. Teotia, S. Kumari, D. Mondal, S. R. Dhakate, *Composites, Part B* **2019**, *160*, 131.
[39] T. Guo, X. Chen, L. Su, C. Li, X. Huang, X.-Z. Tang, *Mater. Des.* **2019**, *182*, 108029.
[40] H. Yang, Z. Yu, P. Wu, H. Zou, P. Liu, *Appl. Surf. Sci.* **2018**, *434*, 318.
[41] H. Yang, Z. Li, H. Zou, P. Liu, *Polym. Adv. Technol.* **2017**, *28*, 233.
[42] Z. Yu, T. Dai, S. Yuan, H. Zou, P. Liu, *ACS Appl. Mater. Interfaces* **2020**, *12*, 30990.
[43] D. X. Yan, H. Pang, B. Li, R. Vajtai, L. Xu, P. G. Ren, J. H. Wang, Z. M. Li, *Adv. Funct. Mater.* **2015**, *25*, 559.
[44] Q. Jiang, X. Liao, J. Li, J. Chen, G. Wang, J. Yi, Q. Yang, G. Li, *Composites, Part A* **2019**, *123*, 310.
[45] D.-X. Yan, H. Pang, L. Xu, Y. Bao, P.-G. Ren, J. Lei, Z.-M. Li, *Nanotechnology* **2014**, *25*, 145705.
[46] L. Zhang, X. Ding, D. Lin, Y. Feng, H. Fu, G. Xiao, P. Xu, Q. Li, *Composites, Part B* **2025**, *297*, 112339.